ARTICLE

Check for updates

Two-photon photocurrent in InGaN/GaN nanowire intermediate band solar cells

Ross Cheriton [1,2,6✉], Sharif M. Sadaf[1,3,4,6], Luc Robichaud[2], Jacob J. Krich [2], Zetian Mi[3,5] & Karin Hinzer [2]

Intermediate band solar cells hold the promise of ultrahigh power conversion efficiencies using a single semiconductor junction. Many current implementations use materials with bandgaps too small to achieve maximum efficiency or use cost-prohibitive substrates. Here we demonstrate a material system for intermediate band solar cells using InGaN/GaN quantum-dot-in-nanowire heterostructures grown directly on silicon to provide a lower cost, large-bandgap intermediate band solar cell platform. We demonstrate sequential two-photon current generation with sub-bandgap photons, the hallmark of intermediate band solar cell operation, through vertically stacked quantum dots in the nanowires. Near-infrared light biasing with an 850 nm laser intensity up to 200 W/cm^2 increases the photocurrent above and below the bandgap by up to 19% at 78 K, and 44% at room temperature. The nanostructured III-nitride strategy provides a route towards realistic room temperature intermediate band solar cells while leveraging the cost benefits of silicon substrates.

[1] Advanced Electronics and Photonics, National Research Council of Canada, 1200 Montreal Rd, Ottawa, ON K1A 0R6, Canada. [2] Centre for Research in Photonics, University of Ottawa, 25 Templeton St, Ottawa, ON K1N 7N9, Canada. [3] Department of Electrical and Computer Engineering, McGill University, 3480 University Street, Montreal, QC H3A 0E9, Canada. [4] Centre Energie, Matériaux et Télécommunications, Institut National de la Recherche Scientifique (INRS), 1650 Boulevard Lionel-Boulet, Varennes, QC J3X 1S2, Canada. [5] Department of Electrical Engineering and Computer Science, University of Michigan, 500S State St, Ann Arbor, MI 48109, USA. [6]These authors contributed equally: Ross Cheriton, Sharif M. Sadaf. ✉email: ross.cheriton@nrc-cnrc.gc.ca

Nanowire-based devices are used for highly tunable III–V optoelectronics grown on affordable, lattice-mismatched substrates, such as silicon. Using III-nitride materials in a nanowire geometry, devices are developed for use as light emitting diodes[1,2], high electron-mobility transistors[3], photodetectors[4], lasers[5–7], and solar cells[8]. In the case of solar cells, attaining high efficiency at a reasonable cost is crucial for a viable platform. With traditional silicon-based solar cells achieving efficiencies of just over 26%[9], they are approaching their fundamental limiting efficiency of around 32%. While traditional solar cells are subject to the Shockley–Queisser limit[10], intermediate band solar cell (IBSC) concepts increase both current and voltage while still using a single junction[11]. Such designs enable the harvesting of energy from sub-bandgap photons through intermediate states deep inside the semiconductor bandgap that act as steppingstones for photogenerated carriers to reach the conduction band while operating at the higher voltage associated with the large bandgap. IBSCs have the potential to reach ultrahigh efficiencies in excess of 45% (and over 60% with concentration[12]), equivalent to a triple-junction solar cell, without the materials, tunnel junctions, number of layers, and cost associated with multijunction solar cells.

The formation of an intermediate band has been pursued using highly mismatched alloys, quantum dot systems and hyperdoping, as outlined in a review by Okada et al.[12] A common route to produce IBSCs is through InAs (0.35 eV) quantum-dot arrays in GaAs (1.4 eV) using established growth processes of the InAs/GaAs quantum-dot system[13]. While InAs/GaAs quantum dots have proven useful for tuning the bandgap of individual subcells in the regime of thermionic carrier escape in multijunction solar cells[14], as IBSC candidates they have sub-optimal theoretical power conversion efficiency[11] and suffer from losses through carrier escape out of the quantum dots at room temperature[15]. Ideally, with a 6000 K black body spectrum, the optimal bandgaps for an IBSC should be 1.95 eV and 0.7 eV under full concentration, and 2.4 eV and 0.9 eV under 1-sun illumination[12]; these high bandgaps are unavailable with most III–V semiconductors. The InGaN/GaN material system supports the ideal bandgap combinations for intermediate band operation[16], has a strong absorption coefficient[17], and also benefits from some commercial maturity from light emitting diode technology. The bandgap of InGaN alloys ranges from 3.4 to 0.7 eV, spanning the solar spectrum and the ideal intermediate band transition energies between bands. InGaN quantum dots in planar GaN on AlN/sapphire substrates have previously demonstrated the sequential two-photon subgap absorption that is the hallmark of intermediate band activity[18].
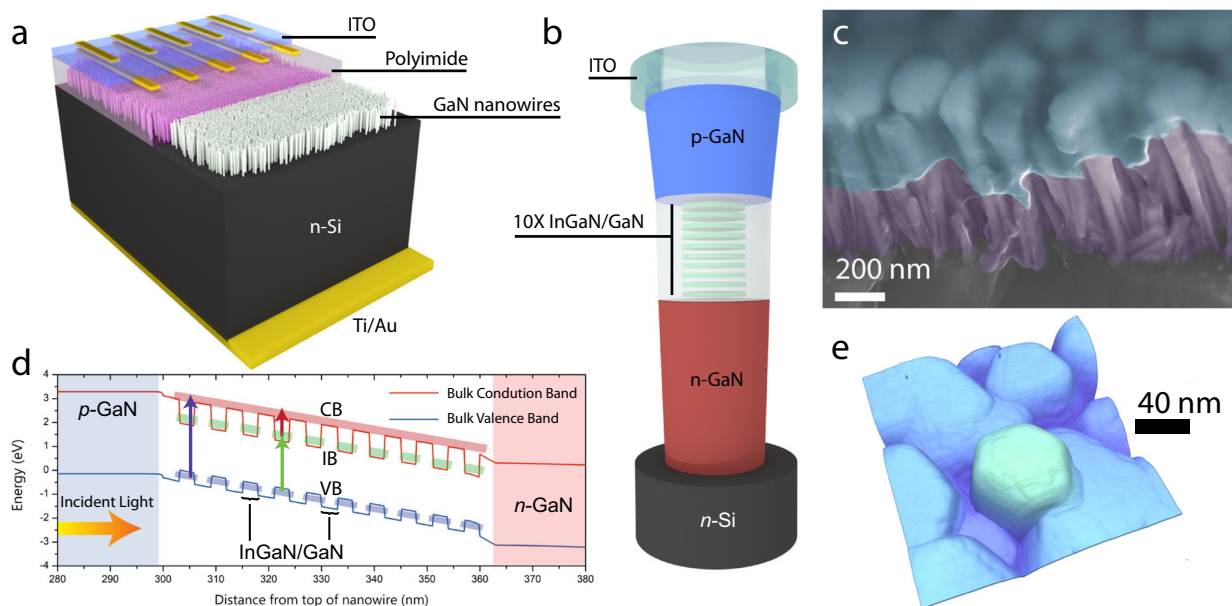
We improve on those results by using InGaN quantum dots inside GaN nanowires on silicon substrates, showing strongly increased sequential two-photon carrier generation while using an inexpensive substrate and higher-indium compositions. The nanowire growth mode removes the need for a lattice-matched substrate and supports vertical stacking of multiple quantum dots without the formation of extended defects[19]. In such a platform, IBSC designs would support higher efficiencies and superior light trapping while retaining the cost advantages of silicon substrates. We demonstrate that the sequential 2-photon subgap photoresponse in our nanowires on silicon is non-thermionic and is significantly stronger than found with ZnTe:O[20], InAs/GaAs[13], GaAs:N[21,22], and even previous InGaN/GaN[18]. We show that this sequential two-photon photocurrent at room temperature is non-thermionic and that with light bias, the solar cells exhibit a 44% increase in photocurrent at room temperature, and a 19% increase in subgap photocurrent at 78 K.

Results

Figure of merit. A necessary condition for an efficient IBSC is for the intermediate band absorber material to have a high figure of merit $v = E_g \mu \tau \alpha^2/q$, where α is the sub-bandgap absorption coefficient, μ is the carrier mobility, τ is the carrier lifetime, E_g is the bandgap, and q is the elementary charge[23,24]. The figure of merit captures the trade-off between increased sub-bandgap absorption and increased carrier recombination due to the introduction of an intermediate band. While an accurate determination of the electron figure of merit requires knowledge of the largely unknown intermediate band to conduction band absorption cross-section, we expect the hole figure of merit for InGaN/GaN systems to be relatively high as a result of the strong bulk material interband absorption ($>5 \times 10^4 \, cm^{-1}$) and large interband transition energies ($>2 \, eV$), despite short nonradiative carrier lifetimes[19] ($\sim 1 \, ns$) and low hole mobilities ($\sim 10 \, cm^2 V^{-1} s^{-1}$).

Nanowire design and geometry. A dense, random ensemble of c-plane nitrogen-face GaN nanowires, each containing ten InGaN quantum dots, was grown by molecular beam epitaxy directly on a silicon substrate, as shown in Fig. 1a–c. The indium composition in the quantum dots varies, ranging up to ~40% with variation between and within nanowires. In the nanowires, the quantum-dot states are inherently decoupled from the conduction and valence band states as a result of strong carrier confinement in the dots. This decoupling of the quantum-dot region is provided by 3 nm barriers of GaN between dots, as shown in the band diagram in Fig. 1d. The quantum dots have diameters of about 40 nm and heights of 3 nm. Transmission electron microscopy and growth details of such nanowires have been previously described with the quantum-dot indium composition studied in great detail[25]. We imaged the nanowires using scanning electron microscopy and atomic force microscopy to assess their morphology, as shown in Fig. 1c, e. The bare hexagonal nanowire ensemble is densely packed with an areal density of 10^{10} nanowires per cm², as shown in Supplementary Fig. 2 with an average nanowire diameter of 89 nm determined statistically in Supplementary Fig. 3. The nanowires are grown without any catalysts and do not rely on substrate patterning techniques that can introduce significant fabrication cost.

Optoelectronic characterization. The emissive properties of the quantum-dot-in-nanowire solar cells are probed through electroluminescence spectroscopy as a function of temperature. An electrical bias of 4 V is chosen to produce significant current in forward bias through the solar cell, for operation as a light emitting diode. The radiative recombination inside the quantum dots allows determination of the transition energies between the confined electron and hole quantum-dot states. Increasing the bias voltage introduces a blueshift of the output spectrum a shown in Supplementary Fig. 4. Electroluminescence spectroscopy at 4 V bias reveals broad emission from the quantum dots from about 550–750 nm (Fig. 2a), indicating a broad distribution of quantum-dot state energies. With reduced temperatures, the electroluminescence reaches a peak at around 200 K at 670 nm. The increase in luminescence with temperature down to 200 K is attributed to the reduction in phonon-assisted recombination of carriers inside the quantum dots nanowires. The decrease in electroluminescence below 200 K is a result of the high magnesium dopant activation energy ($\sim 0.15 \, eV$)[26] which decreases the p-type dopant activation. The electroluminescence spectrum from the nanowire solar cells depends on the indium composition, geometries and dimensions of the quantum dots. The peak of the electroluminescence spectrum is consistent with the radiative

Fig. 1 Cell design and operation. a Schematic of the nanowire solar cell (not to scale) depicting the nanowires grown on silicon and capped with gold and indium tin oxide (ITO) contacts. **b** Individual nanowire structure with a cutaway of the active region for subgap photocurrent generation (not to scale). **c** Cross-sectional scanning electron microscope image of the fabricated nanowire solar cell with ITO in blue, nanowires in violet, and silicon in gray. **d** Simulated band diagram (without polarization effects) at short-circuit highlighting the broadband absorption of light through intermediate states. The electric field is introduced by the *p-i-n* architecture. **e** Atomic force microscopy of the top surface of the nanowire ensemble showing the hexagonal shape of the bare nanowires.

recombination from multiple intermediate levels to the valence band. The broad electroluminescence spectral feature indicates that indium composition fractions can be over 40%, corresponding to an effective bulk InGaN bandgap of ~2 eV.
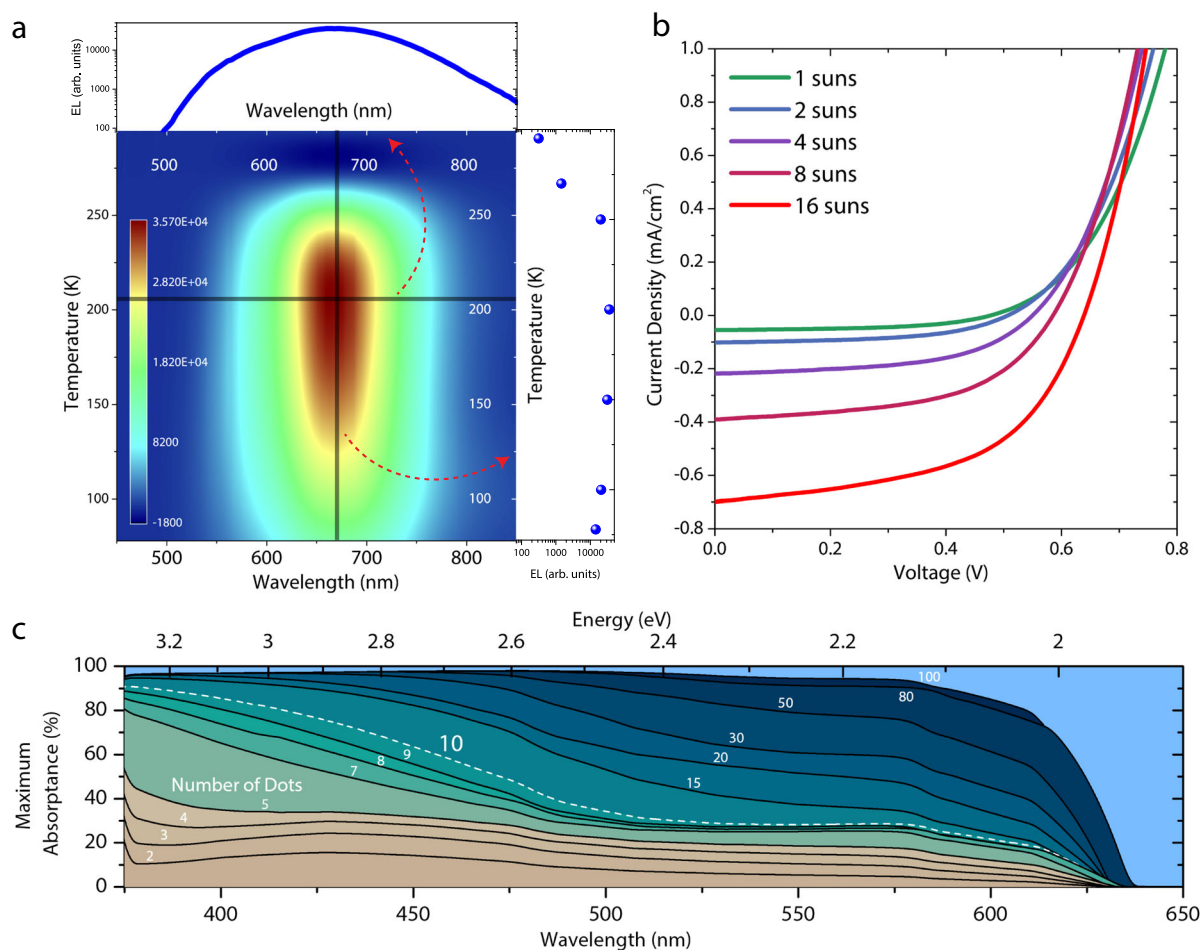
Illuminated current-voltage characteristics are measured as a function of illumination intensity (Fig. 2b). The solar cells show a rectifying characteristic as expected for a *p–n* junction device with a maximum efficiency of 0.016% at 4 suns. Under AM1.5D illumination, the solar cells show a high ideality factor at low illumination conditions prior to decreasing under stronger illumination. This effect may be attributed to a change in recombination from electron- and hole-limiting at low illumination to being only hole-limited at higher injection conditions, due to the effective mass disparity between the two carrier types.

Simulated maximum absorptance. We anticipated the quantum efficiency of these devices to be limited by the quantum-dot sub-bandgap absorption. We constructed a drift-diffusion model of an InGaN/GaN quantum-well device to estimate an upper limit to the sub-bandgap absorptance from the quantum-dot region with ideal miniband transport (Fig. 2c), detailed in Sec. 6 of the Supplementary Information. This model contrasts with our decoupled dots in the fabricated nanowires, which likely exhibit less effective carrier collection than the miniband model. Nevertheless, the model estimates the effects of incomplete absorption on our device performance. The large diameter of the quantum dots leads to a quantum-well-like density of states in the quantum dots. The simulated absorptance for a quantum-dot device is shown in Fig. 2c. The model treats InGaN/GaN multiple quantum wells with the same thicknesses as the experimental dots; the 10-layer configuration corresponds most closely to our experimental devices.

The simulated device absorbs 20–30% of the incident light at wavelengths from 500 to 620 nm. Full devices will require nearly 50–100 quantum dots or light trapping enhancements to achieve sufficient absorption. We estimate an effective bulk absorption

coefficient for the valence band to intermediate band process from the slope of the absorptance vs. number of quantum dots in Fig. 2c, giving a value of approximately 5×10^5 cm^{-1} in a broad range from 500–600 nm. We can use this value to estimate the hole figure of merit v_h to be ~100 (assuming $\tau_h = 1$ ns and $v_h = 10$ cm^2/V·s), which is compatible with high efficiency devices with active regions of length ~500 nm, corresponding to 100 quantum dots per nanowire[24], which is among the highest predicted values of v for any material[23].

Two-photon photocurrent. The hallmark of IBSC operation is current produced by sequential two-photon absorption with energies below the bulk bandgap[12,13,18]. We confirm the existence of a quantum-dot-mediated sequential two-photon absorption process by measuring the quantum efficiency with a chopped tunable wavelength beam and an 850 nm bias light, as described in Fig. 3a, b. While the tunable beam can drive both valence band to intermediate band and intermediate band to conduction band transitions, the light bias can only excite the intermediate band to conduction band transitions (Fig. 3c). In order to be sensitive to the valence band to intermediate band transition, we use a strong light bias, sufficient to promote most carriers in the intermediate band to the conduction band. The experiment is designed to be limited by the valence band to intermediate band absorption process, which requires weak monochromatic, tunable beam at wavelengths less than 600 nm. The infrared bias photons can only be absorbed if intermediate band states are populated after prior absorption of shorter wavelength light. As shown in Fig. 3d, the short-circuit quantum efficiency is maximized at 370 nm, then gradually decreases, yet persists, at wavelengths longer than the GaN bandgap even without the light bias. We identify two possibilities for this last effect. The first possibility is the production of a two-photon photocurrent by a single monochromatic beam. The second possibility is current arising from leakage via defect or surface states in a single-photon absorption process. We observe that the photocurrent increases linearly with tunable beam
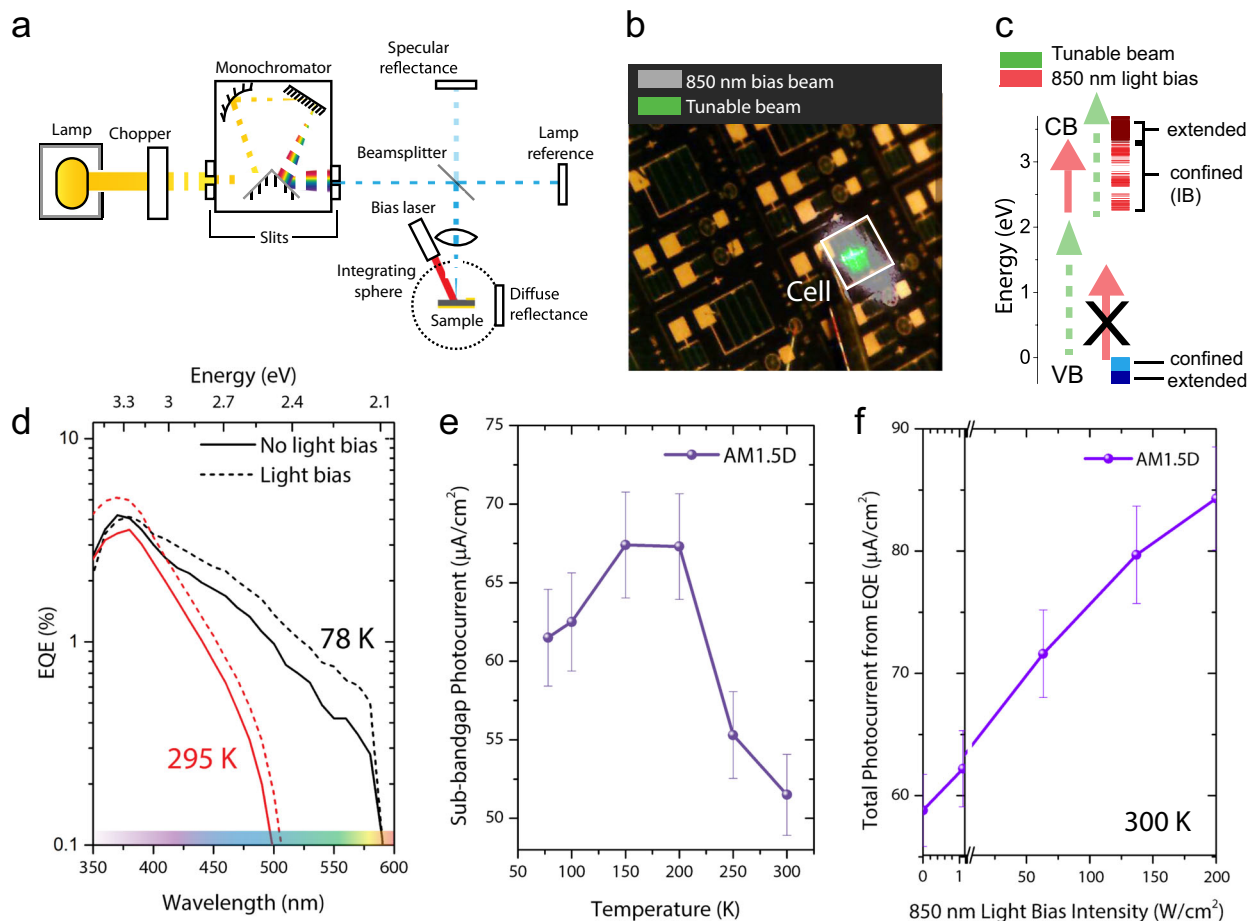
Fig. 2 Optoelectronic characterization and simulation. a Electroluminescence (EL) spectra as a function of temperature with corresponding slices through the center wavelength and temperature of maximized signal. **b** Current-voltage characteristics as a function of AM1.5D illumination up to 16 suns concentration. **c** Simulated absorptance for the valence band to intermediate band transition as a function of incident photon wavelength and number of dots.

intensity, and therefore deem a two-photon photocurrent process to be unlikely without light bias. The low tunable beam intensity rules out both a significant Auger excitation process and a photofilled intermediate band limiting two-photon process. The subgap photocurrent without light bias is therefore attributed to single-photon absorption leakage pathways. A similar subgap photocurrent is also observed in InGaN quantum-well intermediate solar cells on sapphire.[18] With a strong light bias, the photocurrent increases by 44% and 19% at room temperature and 78 K, respectively. At 78 K, this photocurrent increase is predominantly sub-bandgap. Previous observations of sequential two-photon absorption have seen a two-photon signal that is orders of magnitude smaller than the one-photon subgap signal[12,13,18]. The observations in Fig. 3d are the largest sequential two-photon signal of which we are aware.

The increase in photocurrent upon the introduction of the light bias is constrained by the population of already-excited dots, which is expected to be small and biased toward the top few quantum dots of the nanowires. These electrons in the intermediate band are then excited to the conduction band by the strong bias light. Without the bias light, many of those electrons fall back to the valence band before they can be promoted to the conduction band. With a strong light bias, the total possible photocurrent gain is limited by the valence band to intermediate band absorption, by construction of this experiment. Figure 3d shows that shorter wavelengths have a much higher

contribution to the subgap photocurrent with and without the light bias, which we expect for two reasons. Firstly, the absorption is stronger at short wavelengths. Secondly, their absorption occurs near the top of the device. The much higher electron mobility over the hole mobility causes carrier extraction to be significantly more effective near the top of the nanowire where the holes have higher collection efficiency. At room temperature, the light bias induces a strong photocurrent increase at room temperature below 375 nm that does not appear at 78 K. We do not expect the light bias to improve carrier collection for above-gap photons, so the results at 78 K match expectations while the improvement at 295 K is more surprising and is not fully understood, though a similar effect was seen in the other InGaN system studied in ref. [18], at room temperature. The sequential two-photon experiment has been performed using standard methods and the strong subgap two-photon signal is clear[12,13]. Supplementary Fig. 6b shows temperature-dependent external quantum efficiency increases relative to room temperature without light bias. Quantum efficiency reduces with temperature above 200 K, which is not the trend observed in Fig. 3d. The wavelength dependent quantum efficiency as at various temperatures is shown in Supplementary Fig. 6b.

We expect that most of the sequential two-photon photocurrent originates in the top few dots in an uncoupled dot system. A future device can benefit from modulation doping in the quantum-dot region to improve hole transport through the

Fig. 3 Quantum efficiency and photocurrent. a Schematic of the quantum efficiency and reflectivity experimental setup including the laser light bias. **b** Microscope image of the solar cell with the tunable beam (green) and near-infrared light-bias beam (gray) spots. **c** Energy levels and transition energies showing the transitions enabled by the tunable beam and the 850 nm light bias. **d** Short-circuit quantum efficiency at room temperature and 78 K with and without a 200 W/cm^2 light bias in a cryostat. **e** Sub-bandgap (>370 nm) photocurrent as a function of temperature without light bias, calculated from quantum efficiency measurements. Lines are guides to the eye. Error bars indicate estimated errors in photocurrent (±5%). **f** Calculated short-circuit current from the quantum efficiency under AM1.5D illumination as a function of light-bias intensity at 295 K without a cryostat.

quantum dots[27]. Alternatively, reducing the barrier thicknesses to promote miniband conduction through the multiple quantum-dot region can also lead to a more homogenous population of carriers in the intermediate band.

We attribute the sub-bandgap photocurrent increase by the light bias to two-step photon absorption but must rule out alternative mechanisms of tunneling and thermionic emission from dot states. We expect a negligible contribution from tunneling since the higher-indium-fraction dots that contribute to the subgap photocurrent have conduction band states approximately 0.9 eV below the conduction band of GaN, leading to negligible tunneling through the 3 nm GaN barriers. The quantum-dot $k.p$ calculations accounting for the strain and piezoelectric effects in the quantum dots, incorporating indium diffusion, are described in the Supplementary Simulations. To assess the thermionic contribution, we measured the change in photocurrent from wavelengths longer than 370 nm as a function of temperature (Fig. 3e), with the photocurrent calculated from the quantum efficiency measurements. The photocurrent is calculated for the AM1.5D spectrum, which is representative of concentrated sunlight. A solar cell driven by thermionic escape would show an increasing subgap photocurrent with temperature. In contrast, we see the sub-bandgap photocurrent decrease with temperature at temperatures above 200 K. We therefore exclude sample heating from the bias as the origin of the increased

external quantum efficiency signal from light biasing. The decrease in photocurrent below 150 K is consistent with Fig. 2a, which shows p-type carrier freeze-out effects. Calculations in the Supplementary Simulations also show that thermionic escape processes are negligible at the temperature range used in the experiments. Supplementary Fig. 6a shows a similar non-thermionic increase in quantum efficiency with a ~0.1 W/cm^2 red (635 nm) light bias at room temperature, where no appreciable heating to the cell is possible.

Varying the light-bias intensity gives confirmation that the bias is sufficiently strong to make the valence band to intermediate band transition limit the photocurrent. Separate quantum efficiency measurements were performed at room temperature outside the cryostat, as a function of light-bias intensity. The short-circuit current extracted from these quantum efficiency measurements is shown in Fig. 3f. With increasing light bias applied up to 200 W/cm^2, the sub-bandgap quantum efficiency increases by 44% to 114 µA/cm^2, for a total of 77% of the photocurrent being produced from below the bandgap of the host material. The photocurrent in Fig. 3f increases only logarithmically with intensity at the higher intensities, which is consistent with the two-photon process being limited by the valence band to intermediate band absorption, as designed. At light-bias intensities of 200 W/cm^2, the number of bias photons that arrive within the estimated 1 ns hole lifetime is on the order of 100 per nanowire.

Figure 3d also shows single-photon photocurrent without light bias below the bandgap, as in other intermediate band systems[13,18]. This subgap photocurrent is undesirable for IBSC operation, and future devices will need better barriers to ensure carriers are not directly collected from even the first quantum dot.

Discussion

To realize efficient IBSCs, the absorption in the quantum dots must be increased through light trapping and/or adding more quantum dots. Light trapping is the preferable option due to the lower mobility-lifetime product of InGaN/GaN multilayer quantum dots and can increase the filling of the quantum-dot states. While perfectly Lambertian scattering is known to provide a maximum path length enhancement of $4n^2$, where n is the index of refraction, absorption increase via light trapping has been shown to surpass the $4n^2$ limit in certain nanostructures[28]. Such light trapping schemes should therefore be applied to IBSCs whenever possible to reduce the absorber thickness and enhance carrier collection. The interdot transport characteristics can also be improved through miniband formation by promoting interdot tunneling, especially for holes.

In summary, we show that InGaN/GaN quantum-dot-in-nanowire heterostructures on silicon form IBSCs, enabling sub-bandgap current generation on a lower cost platform. We show the strongest relative change in intermediate band quantum efficiency seen to date due to light bias and the first significant intermediate band photocurrent shown on a silicon substrate or with nanowires. Significant sub-bandgap photocurrent enhancement is observed with a near-infrared light bias and does not increase with temperature. These results suggest that wide-bandgap IBSCs can be achieved on a silicon substrate through nanowire geometries. Future investigations are focused on producing optimal InGaN bandgap combinations for the solar spectrum, increasing sub-bandgap absorption in the quantum dots, and reducing nonradiative recombination in the nanowires through optimizations in device design and fabrication.

Methods

Microscopy. Scanning electron microscopy is performed using a Zeiss GeminiSEM 500 at 10 kV accelerating voltage under vacuum. Atomic force microscopy is performed using a Bruker Dimension ICON system using ScanAsyst-AIR probes which have a tip radius of 2 nm.

Growth and fabrication. Self-organized InGaN/GaN dot-in-a-wire heterostructures were grown on n-Si (111) substrates by radio frequency plasma-assisted molecular beam epitaxy (MBE) under nitrogen rich conditions. The substrate surface oxide was desorbed in situ at 770 °C. The growth conditions for Si-doped GaN nanowires included a growth temperature of 750 °C, nitrogen flow rate of 1.0 standard cubic centimeters per minute (sccm), forward plasma power of 350 W, and a Ga beam equivalent pressure of 6×10^{-8} Torr. The InGaN quantum dots were grown at relatively low temperatures (~650 °C) to enhance the In incorporation into the dots. Each quantum dot layer was subsequently capped by a ~3 nm GaN layer. In this experiment, 10 InGaN/GaN quantum dots were incorporated in each GaN nanowire device. The substrate temperature was 750 °C for p-GaN segment subsequently grown after quantum dots. Doping concentration and degeneracy in the p-/n-segments were controlled by the Si (n-type doping) and Mg (p-type doping) effusion cell temperatures. The nanowire device fabrication process included the following steps. First, a polyimide resist layer was spin-coated to fully cover the nanowires, followed by O_2 plasma etching to reveal the nanowire top surface. Thin Ni (8 nm)/Au (8 nm) and Ti (20 nm)/Au (120 nm) metal layers were then deposited on the nanowire surface and the backside of the Si substrates to serve as p- and n-metal contacts, respectively. Subsequently, a 150 nm indium tin oxide (ITO) layer was deposited to serve as a transparent electrode and current spreading layer. The fabricated devices with metal contacts were annealed at ~500 °C for 1 min in ambient nitrogen, and the complete devices with ITO contacts were annealed at 300 °C for 1 h in vacuum. The electric field created in the nominally intrinsic quantum dot region is used to facilitate carrier transport to the quasi-neutral n-type and p-type regions. The nanowires are fabricated into square devices with approximately 1×1 mm, 0.5 mm $\times$ 0.5 mm, and 0.35 mm $\times$ 0.35 mm dimensions as shown in Supplementary Fig. 1.

Low-temperature electroluminescence. The electroluminescence from the nanowire solar cells is measured as a function of temperature inside a Cryo Industries of America liquid nitrogen-cooled cryostat. The cryostat is evacuated to 10^{-3} Pa using a two-stage vacuum pump system. The temperature of the cryostat is controlled to an accuracy of ±5 degrees K with a Cryocon temperature controller, which heated the cryostat sample stage to counteract the cooling from the liquid nitrogen. A small amount of rubber cement is used to secure the sample to the stage. The electrical connection to a specific cell is implemented with a needle probe inside the cryostat wired to a Keithley 2430 sourcemeter. The back of the sample is placed in direct contact with the copper sample stage, which is also wired to the sourcemeter. Emitted light is collected and collimated with an $f = 10$ cm fused silica convex lens and focused into an iHR 320 spectrometer with a 1200 lines/mm grating blazed at 600 nm. Time-dependent electroluminescence current effects were observed as a function of bias voltage, as shown in Supplementary Fig. 9. With lower forward bias voltages, the time to achieve a steady state current increases. Electroluminescence spectra were acquired after multiple minutes to reduce this effect.

Current-voltage characteristics. Illuminated current-voltage characteristics are measured using a four-probe technique to reduce resistance from the wires. A computer controlled Keithley 2430 sourcemeter is used to measure the photo-current and apply the bias voltage during the sweep. The sweep time is set to ~3 seconds from 0 to 3 V. The samples are mounted on a gold-coated temperature-controlled stage. Illumination is provided by a Newport/Oriel solar simulator with a 1600 W xenon arc lamp with a filter to best produce the AM1.5D spectrum. A 1-sun Si reference cell obtained from Newport (Oriel) with NIST traceable certification is used to determine the appropriate 1-sunlight intensity. The variable intensity is achieved through a variety of perforated nickel filters from Spectrolab of known neutral density transmission, which can reduce the incident light intensity of the light to intensities below the unfiltered 16 suns intensity. The spectrum from the Oriel solar simulator is measured with a fibre-coupled ASD FieldSpec spectroradiometer and is shown in Supplementary Fig. 7. The dark current-voltage characteristic demonstrates an on-to-off ratio of 100 and rectify behaviour both shown in Supplementary Fig. 8.

Quantum efficiency. The spot size of the light bias is ~1×1 mm with a primary beam of about 0.5×0.5 mm with a total power of about 300 mW. The source for the primary beam is a 300 W xenon arc lamp filtered through a monochromator to produce a quasi-monochromatic beam from 300 to 1800 nm with a 5 nm spectral width at half maximum. Room temperature quantum efficiency measurements are performed using a Newport IQE-200 quantum efficiency measurement system coupled to a Merlin lock-in amplifier. The primary monochromatic beam is chopped at a frequency of 87 Hz.

For the low-temperature quantum efficiency measurements, the sample is placed on a vertically mounted cryostat cooled with liquid nitrogen, as shown in Supplementary Fig. 5. Sample temperature is measured and maintained with a thermocouple and heater, respectively, both embedded in the copper sample stage. The cryostat is filled with nitrogen and cooled to 78 K. The primary beam is directed onto the sample using a silver mirror. The back contact of the solar cell is electrically connected to a copper cold finger through the mechanical force from a probe needle used to connect to the top contact of the solar cell. The quantum efficiency measurement system is recalibrated to account for the silver mirror and UV-fused silica cryostat window. The continuous wave bias laser beam is incident on the sample at an angle of 10° from the perpendicular axis of the solar cell. A CMOS camera is used to view the overlap of the chopped beam and bias beam on the cell. Beam alignment on the cell is further verified by aligning the electroluminescence emission of the cell to the diffuse reflection of the light-bias beam off the solar cell. The quantum efficiency measurements are performed under short-circuit conditions. Higher temperatures than 78 K are achieved by driving current through the heater, causing liquid nitrogen to boil off and a higher temperature near the sample.

Simulations. The absorption calculation in Fig. 2c is performed with Crosslight APSYS software. The model is based on a standard drift-diffusion semiconductor device coupled to a miniband model for the multiple dot region in the middle of the nanowire. The miniband model is chosen to represent the case that maximizes the transport characteristics in the quantum-dot region, so that transport does not limit device performance. Lifetimes and mobilities are set to high values to achieve near-complete carrier collection of sub-bandgap photons. In this quantum-well approximation, the maximum absorptance can be calculated as a function of wavelength to approximately assess the fraction of light that could be expected to produce photocurrent, assuming the IB to CB transitions are not limiting. The miniband condition is enforced to maximize transport efficiency in an ideal scenario. No reflection at the top surface is allowed, and a virtual contact is placed just below the n^+-GaN base with a reflection condition that corresponds to the refractive index between GaN and silicon. A p^+-GaN top emitter thickness of 300 nm, bottom n^+-GaN base thickness of 270 nm and 1–100 of 3 nm InGaN/3 nm GaN quantum dots are used, as in our nanowires.

References
1. Guo, W., Zhang, M., Banerjee, A. & Bhattacharya, P. Catalyst-free InGaN/GaN nanowire light emitting diodes grown on (001) silicon by molecular beam epitaxy. *Nano Lett.* **10**, 3356–3359 (2010).
2. Nguyen, H. P. T. et al. Engineering the carrier dynamics of InGaN nanowire white light-emitting diodes by distributed p-AlGaN electron blocking layers. *Sci. Rep.* **5**, 34–36 (2015).
3. Li, Y. et al. Dopant-free GaN/AlN/AlGaN radial nanowire heterostructures as high electron mobility transistors. *Nano Lett.* **6**, 1468–1473 (2006).
4. Kind, H., Yan, H., Messer, B., Law, M. & Yang, P. Nanowire ultraviolet photodetectors and optical switches. *Adv. Mater.* **14**, 158–160 (2002).
5. Gradečak, S., Qian, F., Li, Y., Park, H. G. & Lieber, C. M. GaN nanowire lasers with low lasing thresholds. *Appl. Phys. Lett.* **87**, 1–3 (2005).
6. Qian, F. et al. Multi-quantum-well nanowire heterostructures for wavelength-controlled lasers. *Nat. Mater.* **7**, 701–706 (2008).
7. Li, C. et al. Nonpolar InGaN/GaN core–shell single nanowire lasers. *Nano Lett.* **17**, 1049–1055 (2017).
8. Nguyen, H. P. T., Chang, Y. L., Shih, I. & Mi, Z. InN p-i-n nanowire solar cells on Si. *IEEE J. Sel. Top. Quantum Electron.* **17**, 1062–1069 (2011).
9. Yoshikawa, K. et al. Silicon heterojunction solar cell with interdigitated back contacts for a photoconversion efficiency over 26%. *Nat. Energy*, **2**, 17032 (2017).
10. Shockley, W. & Queisser, H. J. Detailed balance limit of efficiency of p-n junction solar cells. *J. Appl. Phys.* **32**, 510 (1961).
11. Luque, A. & Martí, A. Increasing the efficiency of ideal solar cells by photon induced transitions at intermediate levels. *Phys. Rev. Lett.* **78**, 5014–5017 (1997).
12. Okada, Y. et al. Intermediate band solar cells: recent progress and future directions. *Appl. Phys. Rev* **2**, 0–48 (2015).
13. Martí, A. et al. Production of photocurrent due to intermediate-to-conduction-band transitions: a demonstration of a key operating principle of the intermediate-band solar cell. *Phys. Rev. Lett.* **97**, 247701 (2006).
14. Walker, A. W., Theriault, O., Wheeldon, J. F. & Hinzer, K. The effects of absorption and recombination on quantum dot multijunction solar cell efficiency. *IEEE J. Photovoltaics* **3**, 1118–1124 (2013).
15. Antolín, E. et al. Reducing carrier escape in the InAs/GaAs quantum dot intermediate band solar cell. *J. Appl. Phys.* **108**, 064513 (2010).
16. Bhuiyan, A. G., Sugita, K., Hashimoto, A. & Yamamoto, A. InGaN solar cells: present state of the art and important challenges. *IEEE J. Photovoltaics* **2**, 276–293 (2012).
17. Kvietkova, J. et al. Optical investigations and absorption coefficient determination of InGaN/GaN quantum wells. *Phys. Status Solidi* **190**, 135–140 (2002).
18. Sang, L. et al. A multilevel intermediate-band solar cell by InGaN/GaN quantum dots with a strain-modulated structure. *Adv. Mater.* **26**, 1414–1420 (2014).
19. Nguyen, H. P. T. et al. Engineering the carrier dynamics of InGaN nanowire white light-emitting diodes by distributed p-AlGaN electron blocking layers. *Sci. Rep.* **5**, 7744 (2015).
20. Wang, W., Lin, A. S. & Phillips, J. D. Intermediate-band photovoltaic solar cell based on ZnTe:O. *Appl. Phys. Lett.* **95**, 011103 (2009).
21. López, N., Reichertz, L. A., Yu, K. M., Campman, K. & Walukiewicz, W. Engineering the electronic band structure for multiband solar cells. *Phys. Rev. Lett.* **106**, 028701 (2011).
22. Ahsan, N. et al. Two-photon excitation in an intermediate band solar cell structure. *Appl. Phys. Lett.* **100**, 172111 (2012).
23. Sullivan, J. T., Simmons, C. B., Buonassisi, T. & Krich, J. J. Targeted search for effective intermediate band solar cell materials. *IEEE J. Photovoltaics* **5**, 212–218 (2015).
24. Wilkins, M. M., Dumitrescu, E. C. & Krich, J. J. Material quality requirements for intermediate band solar cells. *IEEE J. Photovoltaics* **10**, 467–474 (2020).
25. Woo, S. Y., Bugnet, M., Nguyen, H. P. T., Mi, Z. & Botton, G. A. Atomic ordering in InGaN alloys within nanowire heterostructures. *Nano Lett.* **15**, 6413–6418 (2015).
26. Kumakura, K., Makimoto, T. & Kobayashi, N. Activation energy and electrical activity of Mg in Mg-doped $In_xGa_{1-x}N$ (x<0.2). *Jpn. J. Appl. Phys.* **39**, L337–L339 (2000).
27. Nguyen, H. P. T. et al. p-type modulation doped InGaN/GaN dot-in-a-wire white-light-emitting diodes monolithically grown on Si(111). *Nano Lett.* **5**, 1919–1924 (2011).
28. Yu, Z., Raman, A. & Fan, S. Fundamental limit of nanophotonic light-trapping in solar cells. in *Optics InfoBase Conference Papers* (2010).

Author contributions
K.H. and Z.M. proposed and supervised the research project. The two first authors contributed equally to this research. S.S. performed the growth and fabrication of the nanowires. R.C. performed the experimental characterization and simulation of the nanowire devices. R.C. drafted most of the manuscript with help from S.S., J.K., and K.H. L.R. performed the quantum-dot $k \cdot p$ calculations. J.K. analyzed and guided the interpretation of the experimental data. All authors have provided comments on the manuscript.

Competing interests
The authors declare no competing interests.

Additional information
Supplementary information is available for this paper at https://doi.org/10.1038/s43246-020-00054-6.

Correspondence and requests for materials should be addressed to R.C.

Reprints and permission information is available at http://www.nature.com/reprints

Publisher's note Springer Nature remains neutral with regard to jurisdictional claims in published maps and institutional affiliations.

Supplementary Information – Two-Photon Photocurrent in InGaN/GaN Nanowire Intermediate Band Solar Cells

Ross Cheriton[1,2*], Sharif M. Sadaf[1,3,4*], Luc Robichaud[2], Jacob J. Krich[2], Zetian Mi[3,4], Karin Hinzer[2]

[1]Advanced Electronics and Photonics, National Research Council of Canada, 1200 Montreal Rd, Ottawa, ON, Canada K1A 0R6
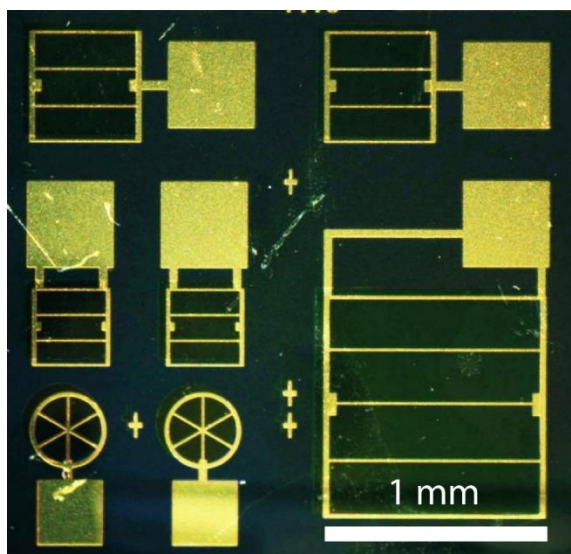[2]Centre for Research in Photonics, University of Ottawa, 25 Templeton St, Ottawa, ON, Canada, K1N 7N9
[3]Department of Electrical and Computer Engineering, McGill University, 3480 University Street, Montreal, Quebec, Canada, H3A 0E9
[4]Department of Electrical Engineering and Computer Science, University of Michigan, 500 S State St, Ann Arbor, MI, USA, 48109
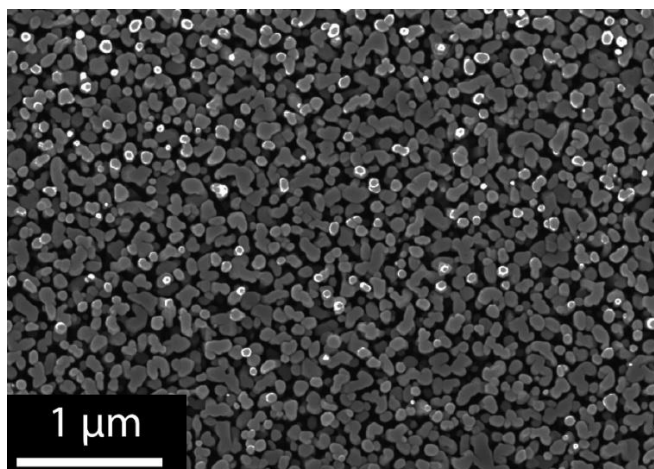*these authors contributed equally to this work
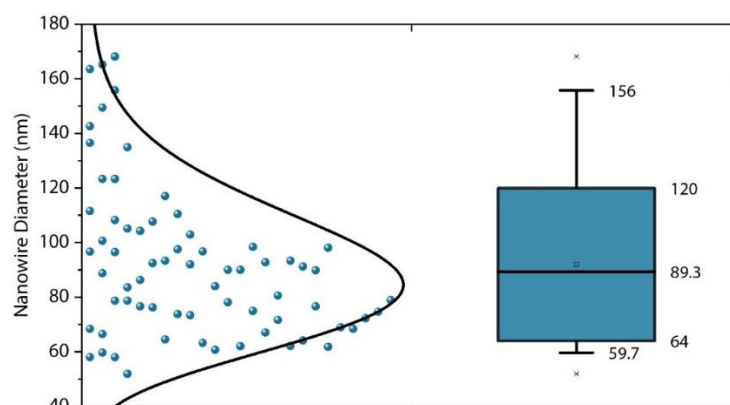
Microscopy

Supplementary Figure 1: Optical microscope images. Optical micrograph of the fabricated nanowire solar cells showing cells of various sizes and geometries. The four smallest cells (lower left of image) are not used for quantum efficiency measurements as the tunable beam spot size is larger than the cell apertures.

Improved intermediate band solar cell performance relies on a high density of intermediate states. The state density can be approximated using knowledge of the state density per quantum dot and the areal density of nanowires. The areal nanowire density, nanowire diameters, and filling fraction are determined from the SEM image in Supplementary Figure 2. The nanowires exhibit roughly hexagonal profiles, with taller nanowires coalescing at the tops of the nanowires. Supplementary Figure 2 is converted to a binary image with a threshold value chosen by inspection to best represent the presence of a nanowire at a certain pixel. The filling fraction is determined to be about 70%. The average diameter of the nanowires is determined by measuring each nanowire diameter in Supplementary Figure 2 manually. The nanowire areal density is determined by counting the number of nanowires in the same top-view SEM image. The diameter statistics are shown in Supplementary Figure 3.
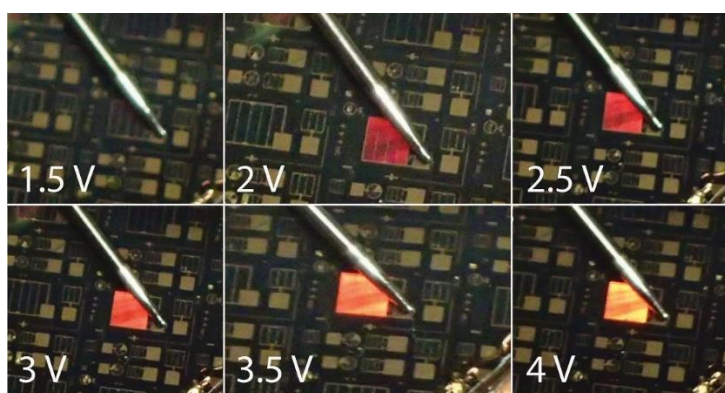
Supplementary Figure 2: Scanning electron microscopy. Plan view scanning electron microscope image of the ensemble of nanowires on silicon prior to planarization with polyimide.
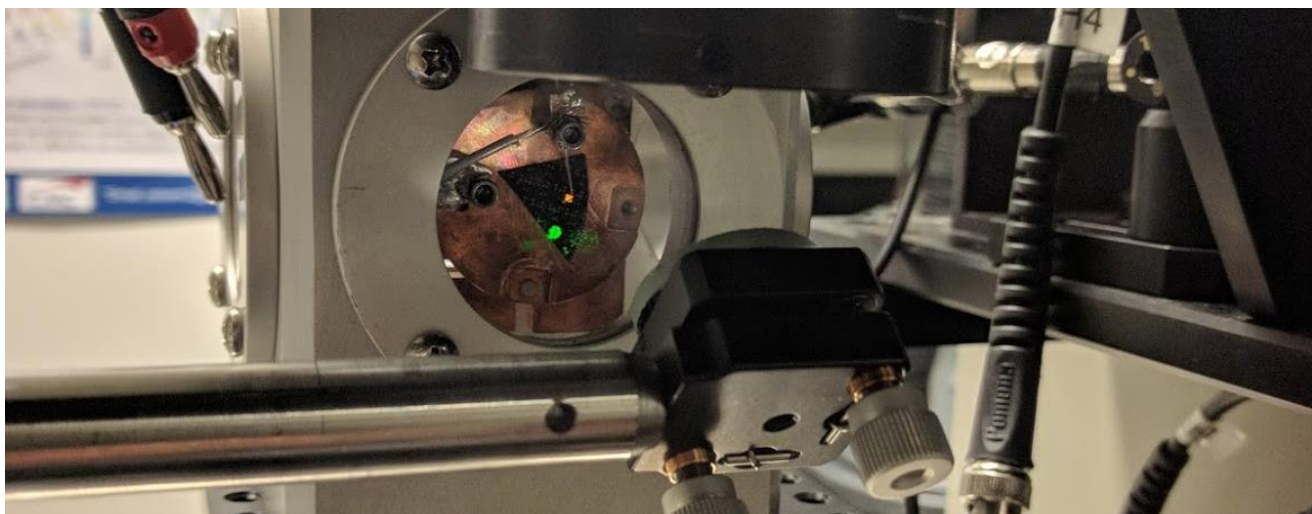

Supplementary Figure 3: Nanowire diameter distribution and statistics. The mean nanowire diameter is 89.3 nm, with extent of the box being the positive and negative standard deviation bounds of the diameters being 120 and 64 nm, respectively. The upper and lower bounds represent the 95% and 5% percentile of the distribution.
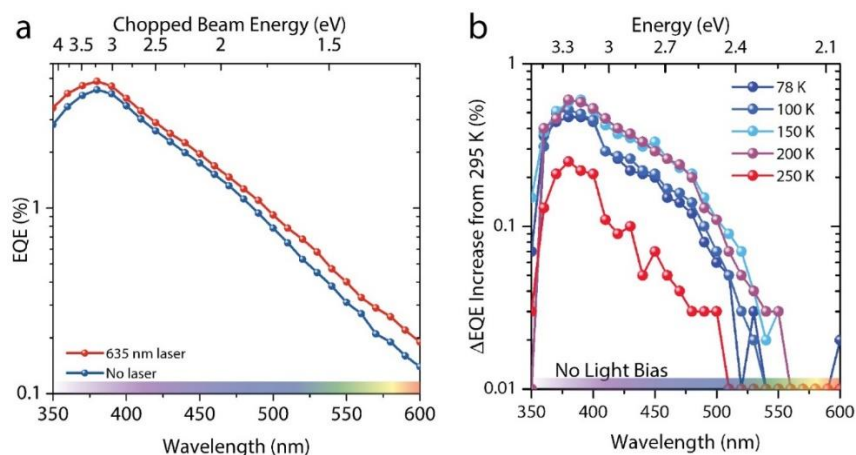
Optical and electrical measurements

Supplementary Figure 4: Electroluminescence. With an increasing voltage bias, the electroluminescence spectrum is blueshifted red to yellow in colour to the human eye. Other samples show a green colour at high bias.
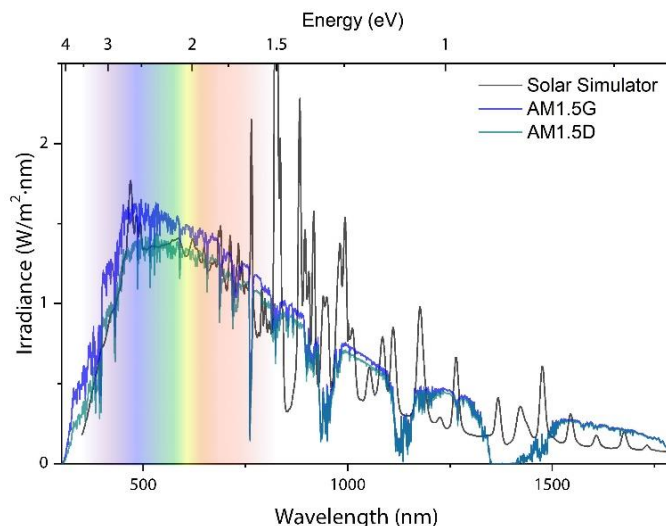
Supplementary Figure 5: Sample mounted in cryostat. The nanowire solar cell mounted vertically in a cryostat. The tunable beam (green) can be aligned to the solar cell (not aligned in image), which is shown luminescing in orange from an applied bias. The mirror (at bottom) is used to divert the tunable beam from the monochromator onto the cell.

The change in quantum efficiency relative to room temperature is shown in Supplementary Figure 6b for a similar but poorer performing sample from a different but nominally identical growth. The quantum efficiency is maximized at 150 K, since it minimizes non-radiative recombination in the quantum dots while still providing dopant activation for improved carrier collection. The long wavelength response is also maximal at 150 K, with higher temperatures leading to a blueshifted response. This shift indicates that quantum efficiency curve does not appreciably redshift as function of temperature, but rather increases in magnitude.

To provide further evidence of the source of the near-gap photocurrent contribution, further quantum efficiency measurements are performed with a weak 635 nm light bias that cannot appreciably heat the solar cell outside the cryostat. A 1.2 mW 635 nm laser (Thorlabs CPS635R) is directed onto the sample at room temperature without a cryostat with a 1 mm^2 spot size. The quantum efficiency with such a laser is shown in Supplementary Figure 6a. Relative increases in the quantum efficiency by around a few percent (relative) are visible at above and below the bandgap of GaN. The low incident power removes the possibility of sample heating being a significant factor in the photocurrent production.
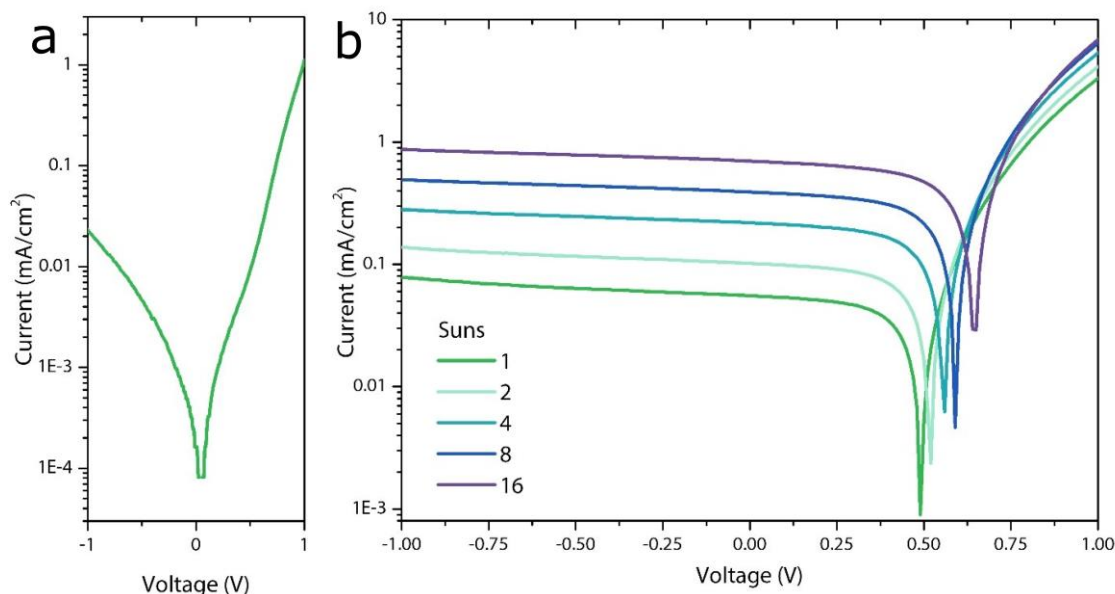

Supplementary Figure 6: Quantum efficiency measurements. a Quantum efficiency as a function of wavelength with and without a weak 635 nm light bias at room temperature. **b** Quantum efficiency relative to room temperature quantum efficiency as a function of wavelength for different temperatures.
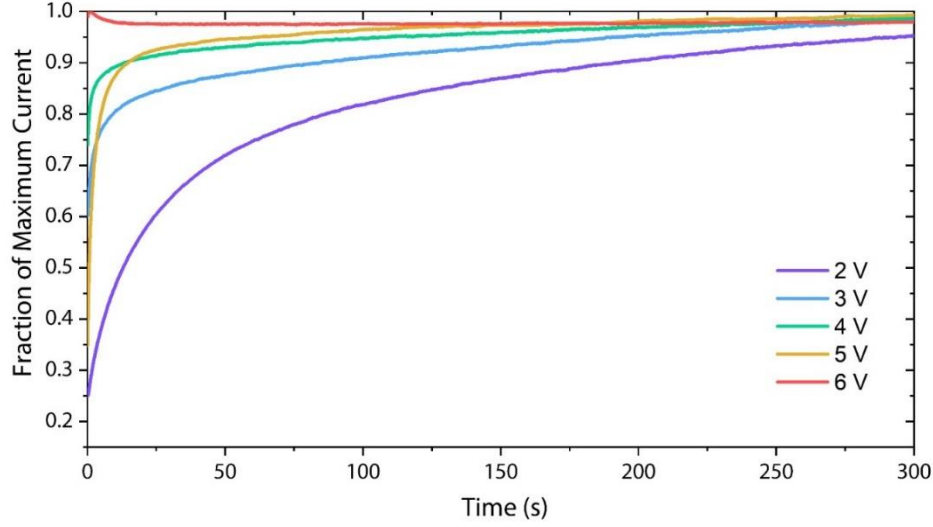
Supplementary Figure 7: Solar simulator spectra. Measured spectra from the Newport Oriel solar simulator compared to the AM1.5D and AM1.5G standard. The solar simulator spectrum is clearly more red-rich than the AM1.5G or AM1.5D solar spectrum, leading to the underestimation of the photocurrent from illuminated current-voltage curves. A more accurate photocurrent measurement is determined through quantum efficiency measurements in the main text (Figure 3d) and provides a value of 79 μA/cm2, which is higher than the current-voltage determined photocurrent (68 μA/cm^2).

The absolute values of the current-voltage characteristics are measured in the dark at room temperature, as shown in Supplementary Figure 8. The solar cells demonstrate little leakage current in reverse bias. The dark current at -1 V (reverse bias) is less than 25% of the photocurrent produced at 1 sun. At 16 suns illumination, the dark current is less than 3% of the total photocurrent. The difference between the photocurrent and dark current is shown in Supplementary Figure 8b. The low reverse bias current indicates that the *p-i-n* junction in the nanowire solar cell is effective at charge separation and that the leakage current is not proportional to the incident light intensity. As a higher reverse bias leakage current would imply carrier tunneling or thermionic escape, this further establishes that our intermediate band solar cell is not driven by these processes, but rather the intermediate band solar cell process.

Supplementary Figure 8: Dark-current voltage characteristics. a. Dark current-voltage characteristics of the solar cell measured at room temperature. **b**. Difference between the photocurrent and dark current with increasing solar illumination intensities as a function of bias voltage.
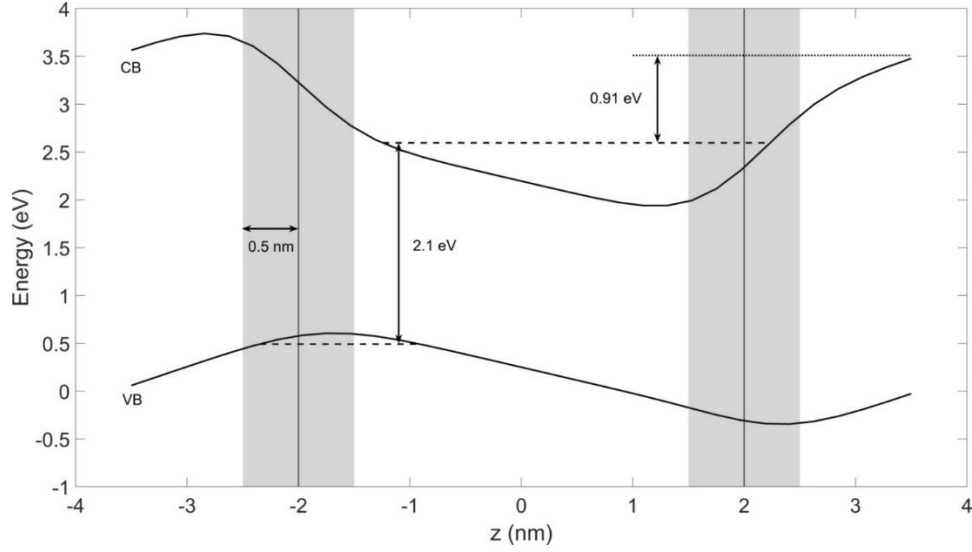
Supplementary Figure 9. Time-varying current effects. The fraction of maximum current as a function of time for a nanowire solar cell under various applied biases at 295 K. low forward bias, the solar cells required more time to reach their maximum current. At higher biases, the solar cells reach their stable current more rapidly. At 6 V, the nanowires reverse the trend and the current decreases slightly over time until it reaches equilibrium. We believe these behaviours are due to heating effects under bias in the sample. This effect is only seen during electroluminescence and not when producing photocurrent, where the current density is over 100 times lower.

Simulations

To better understand experimental results, we have performed electronic structure calculations for the InGaN/GaN quantum dot system. These calculations indicate what subgap optical transitions to expect from the device as well as show if we should expect intermediate-to-conduction band thermionic emission. Electron and hole states are calculated using $k \cdot p$ theory in the envelope function approximation to provide single-particle energy levels[1]. We have used an 8-band model, which includes spin-orbit coupling and crystal field splitting for wurtzite InGaN alloys[2]. The calculation has hexagonal periodic boundary conditions, leading to a quantum dot superlattice[3,4]. Using an approach that allows the use of different electronic and strain unit cells, we can remove dot-to-dot interactions[4]. We study cylindrical dots and have chosen our unit cells such that the dots are completely uncoupled in the xy-plane, but still coupled in the growth direction (z), as is the case in our nanowires. We implement smooth indium profiles by convolving sharp indium profiles with a Gaussian, effectively modelling indium diffusion observed in the devices. Dots are characterized by their radius, height, indium fraction and smoothing kernel. The barrier is taken as pure GaN, which is then modified by smoothing. The experimental QD array has period 7 nm and smoothly varying indium profiles, which we approximate with dots of height 4 nm and smoothing of 0.5 nm in the growth direction. The combined effects of the piezoelectric potential and indium diffusion lead to strongly deformed electron and hole confining potential wells compared to the idealized dots sketched in Figure 1d, as shown in Supplementary Figure 10. We extract the lowest electron and hole state energies, which we use to define the two subgap transitions of the QD. Both states are converged numerically within a 5 meV error. From Supplementary Figure 10, we see that the QD system has an optical subgap of 2.1 eV. In the full device, electrons in the CB must be extracted through fully relaxed GaN, setting the barrier to extract electrons out of the QD layers at the GaN CB, which is 3.51 eV, indicated by the dotted line in Supplementary Figure 10. Dots in the experimental devices have a range of indium fractions and sizes.

In the two-photon QE experiments, the bias light must have photon energy greater than the 0.91 eV indicated in Supplementary Figure 10 in order to contribute to current at the contact. The 0.91 eV barrier is sufficiently large to rule out thermionic emissions in current generation for the range of studied temperatures. Between 77 K and 295 K, thermionic emission would be increased by a factor of ten[45], which is not observed in Figure 3e. Carrier tunneling outside the quantum dot region is also not possible as there are no states to tunnel to from the lowest confined quantum dot states, as shown in Figure 1d. The tunneling process requires a state with nearly identical energy and sufficiently thin barrier; in our device we have neither of these conditions.

Supplementary Figure 10: Electronic structure of an array of cylindrical InGaN QD's in GaN, including indium diffusion, deformation potentials, and piezoelectric potentials. Solid lines are the bulk conduction and valence band edge energies, including the local piezoelectric potential on a cut through the growth axis of the dot. Dashed lines show the lowest energy electron/hole confined states in the quantum dots. Dotted line shows the bulk conduction band edge energy of GaN, which is the energy level required to extract an electron. Double arrows show the two subgap optical transitions that contribute to photocurrent. The QD has a 4 nm height, 20 nm radius, 45% indium with a 0.3 nm smoothing kernel in the *xy*-plane and 0.5 nm in the *z*-direction. Vertical lines indicate the nominal QD height and grey bands the standard deviation of the smoothing kernel.

References

1. Willatzen, M. & Lew Yan Voon, L. C. *The k p method: Electronic properties of semiconductors*. *The k p Method: Electronic Properties of Semiconductors* (2009).
2. Winkelnkemper, M., Schliwa, A. & Bimberg, D. Interrelation of structural and electronic properties in InGaN/GaN quantum dots using an eight-band k·p model. *Phys. Rev. B* **74**, 155322 (2006).
3. Vukmirović, N., Ikonić, Z., Indjin, D. & Harrison, P. Symmetry-based calculation of single-particle states and intraband absorption in hexagonal GaN/AlN quantum dot superlattices. *J. Phys. Condens. Matter* **18**, 6249–6262 (2006).
4. Vukmirović, N. & Tomić, S. Plane wave methodology for single quantum dot electronic structure calculations. *J. Appl. Phys.* **103**, (2008).